



Nanoscale

**Boosting Cycling Stability of Ni-rich Layered Oxide Cathode
by Dry Coating of Ultrastable Li₃V₂(PO₄)₃ Nanoparticles**

Journal:	<i>Nanoscale</i>
Manuscript ID	NR-COM-11-2020-008305.R1
Article Type:	Communication
Date Submitted by the Author:	05-Jan-2021
Complete List of Authors:	Wang, Dongdong; Tianjin University; University of California, San Diego, NanoEngineering Yan, Qizhang; University of California, San Diego, NanoEngineering Li, Mingqian; University of California, San Diego, NanoEngineering Gao, Hongpeng; University of California San Diego Tian, Jianhua; Tianjin University, Shan, Zhongqiang; Tianjin University, School of Chemical Engineering and Technology Wang, Ning; Hebei Normal University, Luo, Jian; University of California at San Diego, NanoEngineering Zhou, Meng; New Mexico State University, Chen, Zheng; University of California, San Diego, NanoEngineering

SCHOLARONE™
Manuscripts

Boosting Cycling Stability of Ni-rich Layered Oxide Cathode by Dry Coating of Ultrastable $\text{Li}_3\text{V}_2(\text{PO}_4)_3$ Nanoparticles

Dongdong Wang,^{a,b} Qizhang Yan,^a Mingqian Li,^{a,c} Hongpeng Gao,^d Jianhua Tian,^b Zhongqiang Shan,^b Ning Wang,^{a,e,*} Jian Luo,^{a,c,d,f} Meng Zhou,^g and Zheng Chen^{a,c,d,f*}

^aDepartment of NanoEngineering, University of California San Diego, La Jolla, CA 92093

^bSchool of Chemical Engineering and Technology, Tianjin University, Tianjin 300350, P. R. China

^cProgram of Chemical Engineering, University of California San Diego, La Jolla, CA 92093

^dProgram of Materials Science and Engineering, University of California San Diego, La Jolla, CA 92093

^eAnalysis and Testing Centre, Hebei Normal University, Shijiazhuang 050024, P. R. China

^fSustainable Power and Energy Center, University of California San Diego, La Jolla, CA, 92093, United States

^gDepartment of Chemical and Materials Engineering, New Mexico State University, Las Cruces, NM 88003, United States

*Correspondence to: zhengchen@eng.ucsd.edu; hebsjzwn@gmail.com

Abstract

Nickel (Ni)-rich layered oxides such as $\text{LiNi}_{0.6}\text{Co}_{0.2}\text{Mn}_{0.2}\text{O}_2$ (NCM622) represent one of the most promising candidates for the next-generation high-energy lithium-ion batteries (LIBs). However, the pristine Ni-rich cathode materials usually suffer from poor structural stability during cycling. In this work, we demonstrate a simple but effective approach to improve the cycling stability of NCM622 cathode by dry coating of ultrastable $\text{Li}_3\text{V}_2(\text{PO}_4)_3$ -carbon (LVP-C) nanoparticles, which leads to a robust composite cathode (NCM622/LVP-C) without sacrificing specific energy density compared with pristine NCM622. The optimal NCM622/LVP-C composite presents a high specific capacity of 162 mA h g^{-1} at 0.5 C and excellent cycling performance with 85.0 % capacity retention after 200 cycles at 2 C, higher than that of the pristine NCM622 (67.6%). Systematic characterization confirms that the LVP-C protective layer can effectively reduce the side reactions, restrict the cation mixing of NCM622 and improve its structural stability. Moreover, the NCM622/LVP-C||graphite full cells also show a commercial-level capacity of 3.2 mA h cm^{-2} and much improved cycling stability compared with NCM622/LVP-C||graphite full cells, indicating the great promise for low-cost, high-capacity and long-life LIBs.

Keywords: Ni-rich cathode, $\text{Li}_3\text{V}_2(\text{PO}_4)_3$, dry coating, high stability, lithium-ion batteries

1. Introduction

The wide-spread applications of lithium-ion batteries (LIBs) in electronic devices, electric vehicles (EVs), and grid energy storage have driven an increasing demand for electrode materials with higher energy density, better rate capability, and longer cycling stability.¹⁻⁵ Owing to the high capacity and reduced cost, layered Ni-rich $\text{LiNi}_{1-x-y}\text{Co}_x\text{Mn}_y\text{O}_2$ (NCM, $0 < x, y, z < 1, 1 - x - y \geq 0.6$) is becoming the dominating cathode material in the state-of-the-art LIBs.⁶⁻⁸ Among them, $\text{LiNi}_{0.6}\text{Co}_{0.2}\text{Mn}_{0.2}\text{O}_2$ (NCM622) displays a high reversible capacity of 170 mA h g^{-1} in the voltage range from 3.0 to 4.3 V (vs. Li/Li^+) and carries reasonably good thermal stability, rendering it one of the most promising candidates for the next generation of advanced high-energy LIBs.⁹ However, the as-synthesized Ni-rich cathode materials usually suffer from Li/Ni mixing and high residual Li components ($\text{Li}_2\text{CO}_3/\text{LiOH}$) on the particle surface, reducing the initial Coulombic efficiency and discharge capacity.¹⁰⁻¹² Meanwhile, irreversible phase transformation and loss of lattice oxygen of the cathode materials during the delithiation/lithiation process, accompanied by side reactions with the electrolyte, often leads to poor cycling performance.¹³⁻¹⁵ These problems hinder the wider range of applications for these high-energy Ni-rich cathode materials. On-going efforts on improving cycling performance of NCM622 cathodes have been focused on establishing protective coating or doping that can stabilize the particle morphology and structure, such as Al_2O_3 , TiO_2 , LiNbO_3 , $\text{Li}_{1.3}\text{Al}_{0.3}\text{Ti}_{1.7}\text{PO}_4$ (LATP).¹⁶⁻²⁰ While these coating materials have demonstrated improved cycling stability on NCM622, they do not contribute to charge storage and also sacrifice capacity or rate performance due to extra ionic resistance added onto the electrode particles.

Recent studies showed that building a surface coating layer of olivine phase LiMPO_4 , ($\text{M} = \text{Fe}, \text{Mn}, \text{etc.}$) such as LiMPO_4 could be an effective approach to enhance electrochemical properties of Ni-rich layered oxides.^{21,22} However, previous approaches on building such type of coating materials have been based on solution process followed by high-temperature annealing process, which potentially raises cost concerns due to the complication synthesis. More importantly, for high Ni cathode such as NCM622, solution process with annealing commonly induces side reactions such as Li loss, cation (Li^+/Ni^+) mixing and surface passivation, which deteriorates the intrinsic properties of the high-Ni cathode materials.

On the other hand, the monoclinic $\text{Li}_3\text{V}_2(\text{PO}_4)_3$ (LVP) has also attracted great attention as a

promising cathode material owing to its excellent cycling performance, low cost, high thermal stability, good safety and higher operation voltage compared with LiFePO_4 .²³⁻²⁵ Although LVP-based cathode materials have a relatively low theoretical capacity of 133 mA h g^{-1} when charged up to 4.3 V (vs. Li/Li^+),²⁶ previous studies show that carbon-coated LVP cathodes could maintain ultra-long cycling stability of without obvious capacity decay (e.g., 2000 cycles), comparable to LiFePO_4 cathodes.²⁷⁻²⁹ However, the charge/discharge voltage curves of LVP cathodes usually present multiple redox plateaus during cycling process, resulting in potential challenges in matching with anode materials and monitoring the state-of-charge (SOC) of the cells, which limits its commercial applications.^{30, 31}

Herein, we show a promising strategy to achieve stable and high-performance composite cathode by combining nanoparticulate LVP particles and microspherical NCM622 via a facile dry coating process. In this composite cathode (NCM622/LVP), the surface of NCM622 microspheres was uniformly coated by LVP nanoparticles via a simple drying mixing process without destructing the secondary structure of NCM622 microspheres. This approach effectively mitigates the intrinsic stability problem of pristine NCM622 and the voltage and capacity limitations of LVP cathode while maintaining the desired properties of the two constituents. Integrating the two cathode materials is effective in enhancing the cycling stability and rate capability of NCM622 cathode materials without sacrificing the energy density of the entire cathode. Owing to the protective effect of the LVP layer, the cation mixing and irreversible phase transformation of NCM622 cathode during the cycling process is reduced and restricted, enhancing the structural stability. In addition, with the controlled amount of LVP, the NCM622/LVP cathode eliminates the multiple charge-discharge plateaus of LVP, making it easier for SOC monitoring. We also show that such NCM622/LVP composite cathode can maintain higher specific capacity than NCM622 cathode (85.0 % vs. 67.6 %) after 200 cycles at 2 C in 3.0-4.3V (vs. Li^+/Li). Moreover, NCM622/LVP||graphite full cells with a high capacity of 3.2 mA h cm^{-2} also showed a capacity retention of 89.1% after 100 cycles at 0.5 C, higher than that of NCM622||graphite full cells (56.4 %). This work demonstrated a new avenue for developing low-cost, high energy, and long-life LIB cathodes.

2. Experimental Section

2.1 Materials Preparation

The LVP nanoparticles with conductive carbon coating were prepared via a sol-gel method.³² In a typical synthesis, 0.1819 g of V_2O_5 , 0.3781 g of $H_2C_2O_4 \cdot 2H_2O$ were dissolved in 5 mL of distilled water at room temperature. The solution was then heated and stirred at 80 °C with a silicon oil bath. After heating and stirring for 1 h, 0.1108 g of Li_2CO_3 and 0.3451 g of $NH_4H_2PO_4$ were added to the previous solution. After another hour of heating, a gel was formed. When the water was completely evaporated, the dried LVP powder was transferred into an agate mortar and pouring with phenolic resin solution (10 wt.%). After grinding for 20 min, the mixture was calcined at 800 °C for 8 h in argon atmosphere with a heating rate of 5°C/min. Finally, the LVP nanoparticles with carbon coating (LVP-C) were obtained after the ball milling for 30 minutes.

To make the composite cathode, commercial NCM622 (BTR Corporation) and the as-synthesized LVP-C nanoparticles were placed in the mortar and grinding for 0.5 h. Then the samples were transferred to 20 mL vials and mixed for 0.5 h via a XH-C Vortex mixer with 1000 rpm/min. NCM622/LVP-C composites with different LVP-C loading (5wt.% to 30wt.%) were obtained by adjusting weight ratios between the two components. The porosity of each sample was calculated by comparing the actual density and the bulk density of each constituent.

2.2 Materials Characterization

The morphology of different samples was examined by Ultrahigh Resolution Scanning Electron Microscope (UHR-SEM, FEI XL30). Microstructural information and crystal characteristics of the samples were examined by Transmission Electron Microscopy (TEM, FEI Titan 80-300 kV S/TEM, America) images and selected area electron diffraction (SAED). High-resolution TEM (HR-TEM) was recorded on a field emission gun JEOL-2800 at 200 kV with Gatan OneView Camera (full 4 K x 4K resolution). Thermogravimetric analysis (TGA) was performed on an SDTA851E thermoanalyzer between room temperature and 800 °C with a heating rate of 10 °C min⁻¹. Crystallographic structures of the samples were confirmed by X-ray diffraction (XRD) using Cu K α radiation in the region of $2\theta = 10-80^\circ$ at 30 kV and 10 mA (Bruker D2 Phaser, Germany).

2.3 Electrochemical Measurement

The cathode electrodes were fabricated by casting the slurry of active materials (NCM622, LVP or NCM622/LVP composites), Super-P, and poly (vinylidene fluoride) (PVDF) binder with a mass ratio of 8:1:1 in N-methyl-2-pyrrolidone (NMP) solvent on Al foil, and then dried at 120 °C for 12 h

in a vacuum oven before use. The graphite electrodes (MTI corporation, **Figure S1**) were fabricated by casting the slurry of active materials, Super-P, and PVDF with a mass ratio of 90:5:5 in NMP solvent on Cu foil, and then dried at 80 °C for 8 h in a vacuum oven before use. CR-2032 type coin cells were assembled to evaluate the electrochemical properties of all the samples. The electrolyte was 1 M LiPF₆ in a mixture of ethylene carbonate (EC)/diethyl carbonate (DEC) with a volume ratio of 1:1. Celgard 2400 microporous polypropylene membrane was used as the separator. For half cells, the mass loading of cathode electrode was controlled at 5 mg cm⁻². For full cells, the mass loading of cathode electrode was controlled at 20 mg cm⁻². The negative to positive capacity ratio (N/P ratio) of the full cells was controlled at 1.2. Thus, the rate and specific capacity values of full cells were calculated based on the cathode mass. All cells were assembled in a glovebox filled with argon gas (O₂ and H₂O levels < 0.1 ppm). NEWARE battery testers were used to perform constant current charge-discharge cycling in the voltage range of 3.0-4.3 V (vs. Li⁺/Li) for half-cells and 2.8-4.2 V for full cells. Cyclic voltammetry (CV) was measured using a Metrohm Autolab electrochemical workstation between 3.0 and 4.3 V (vs. Li⁺/Li) with different scan rates. Electrochemical impedance spectroscopy (EIS) measurements were acquired in the frequency range with 0.1-10⁵ Hz and a perturbation voltage of 5 mV.

3. Results and Discussions

The LVP nanoparticles with conductive carbon coating were first synthesized by a sol-gel method for the preparation of composites cathodes. **Figure S2a** and **b** show that the carbon-coated LVP (LVP-C) nanoparticles have a relatively uniform grain size of 100-200 nm. The HR-TEM image of LVP-C shows an amorphous surface carbon layer with a thickness of about 8 nm. In the bulk material, the lattice fringes have a typical spacing of 0.365 nm, which can be assigned to (211) plane of LVP (**Figure S2c**).³³ Furthermore, the SAED pattern confirms that the monoclinic Li₃V₂(PO₄)₃ phase is successfully produced (**Figure S2d**). XRD pattern displays that LVP-C nanoparticles can be well indexed to a monoclinic structure phase (JCPDS No. 97-009-6962) with a space group of *P21/n*. No diffraction peak of carbon appeared, indicating that the residual carbon is mainly amorphous (**Figure S3a**).³⁴ TGA also presents that the carbon content of LVP-C nanoparticles is 4.04% (**Figure S3b**). The SEM morphologies of NCM622/LVP-C composites with different LVP-C contents are shown in **Figure S4**. When the LVP-C content was 5 wt.%, a significant portion of the NCM622 surface was still exposed,

indicating the loading of LVP-C nanoparticles was too little to form a protective coating layer (**Figure S4a, 3b**). When the LVP-C content increased to 20 wt% and 30 wt%, although the NCM622 surface was completely covered by LVP-C nanoparticles, the aggregation of additional LVP-C nanoparticles occurred on the surface of the NCM622 particles (**Figure S4c, 3f**). Therefore, the optimal LVP-C content in the composite was determined at 10 wt.%. As shown in **Figure 1**, NCM622 materials were spherical particles with a diameter of 3-10 μm consisted of densely packed primary nanoparticles of 200-800 nm (**Figure 1a, 1b**). After dry coating of LVP-C nanoparticles, the optimal NCM622/LVP-C composites still showed the spherical micron-sized particles, which were covered uniformly with LVP-C nanoparticles on the surface without excess LVP-C nanoparticles agglomerated (**Figure 1c, 1d**).

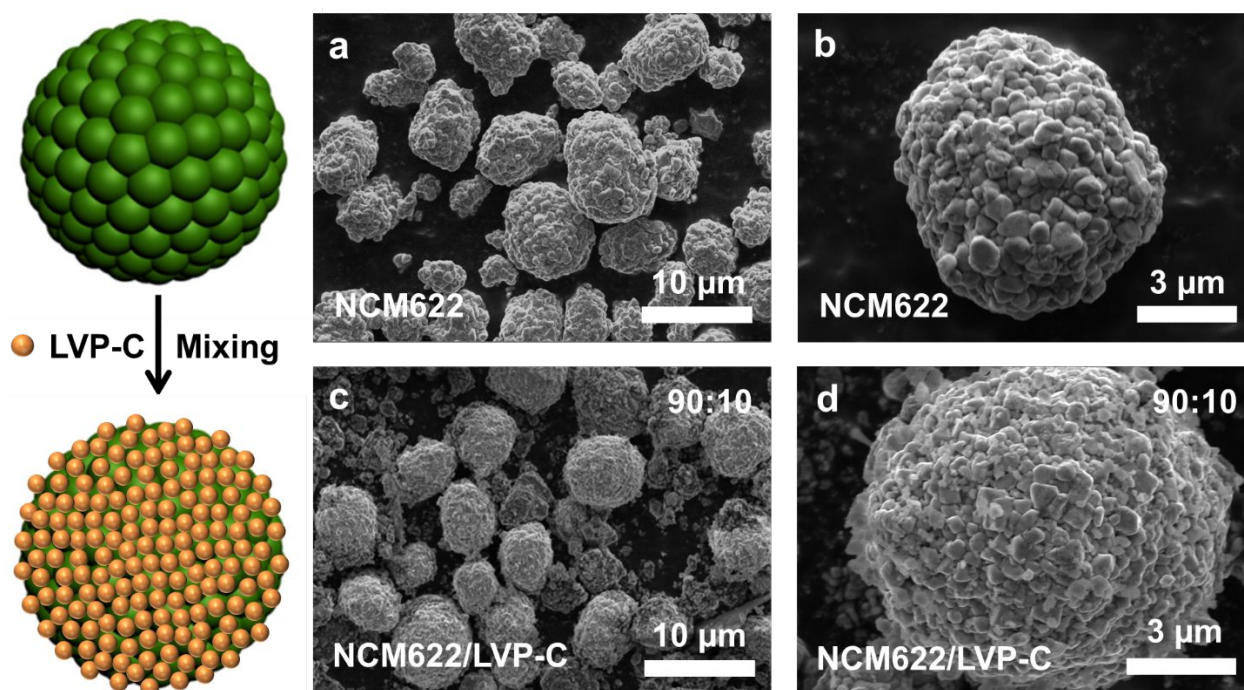


Figure 1 SEM images of (a, b) the NCM622 and (c, d) the NCM622/LVP-C composites with 10 wt.% of LVP-C coating.

Figure 2 shows the cross-sectional SEM images of the two different electrodes with a loading of 20 mg cm^{-2} . The NCM622 electrode displays that the micron-sized particles are relatively uniformly mixed with the super-P and binder with a clear porosity (**Figure 2a, 2b**). After coating with the LVP-C nanoparticles on NCM622 surface, the stacking pores are more completely filled with some LVP-C nanoparticles, leading to the higher tap density of NCM622/LVP-C electrode (**Figure 2c, 2d**). **Table**

1 summarizes that the NCM622/LVP-C electrode has a smaller porosity than NCM622 electrode (27% vs. 31%), leading to a slightly enhanced volumetric energy density due to the LVP-C coating.

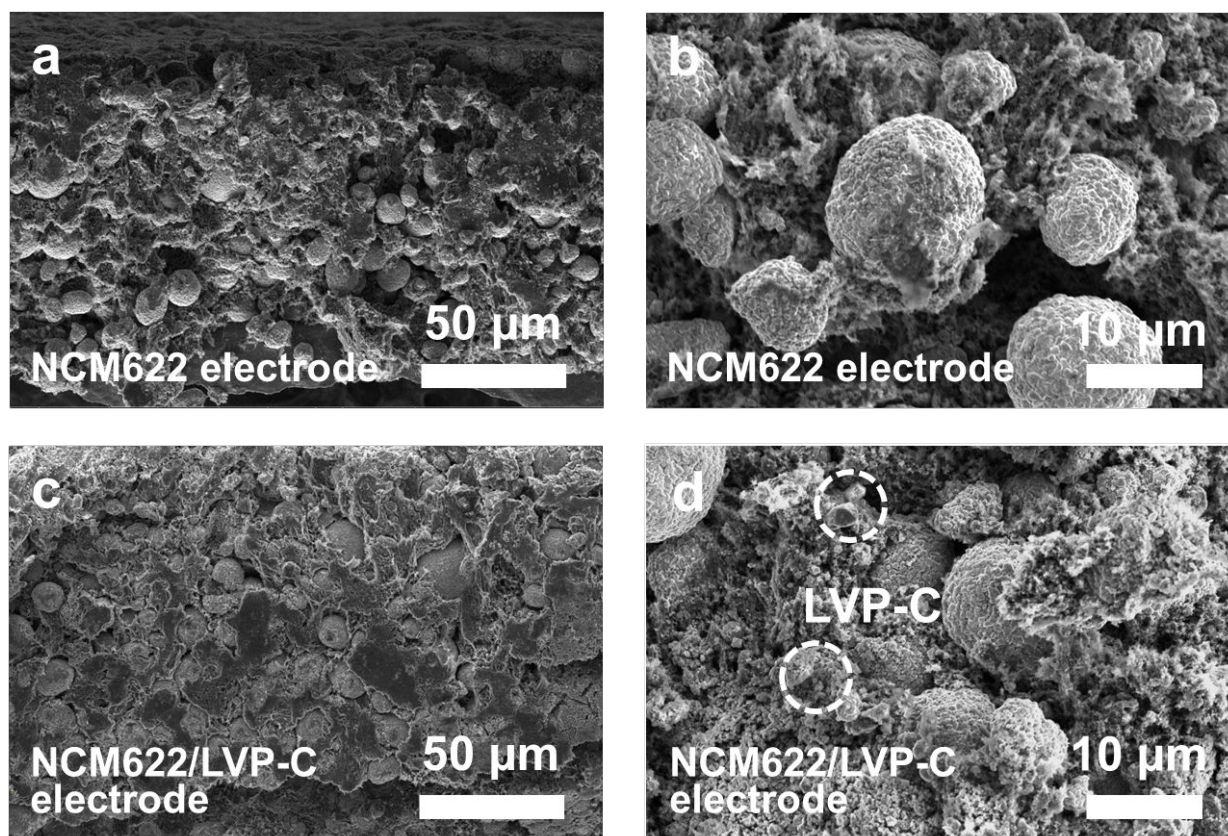


Figure 2 Cross-sectional SEM images of the NCM622 electrode (a, b) and the NCM622/LVP-C electrode (c, d).

Table 1 Summary of porosity of two electrodes.

Electrodes	NCM622/LVP	NCM622
Porosity	27%	31%

The electrochemical performance of different electrodes was first examined using half-cell configuration using coin cells. **Figure 3a** shows that while the NCM622/LVP-C electrode has a slightly lower specific capacity than NCM622 electrode in the initial 50 cycles at 0.5 C charge/discharge, it can retain a higher capacity after 100 cycles owing to the LVP-C protective layer (97.2% vs. 91.0%). Furthermore, a high average coulombic efficiency (CE) of 99.7% was obtained

during the 100 cycles. In addition, the cycling performance of NCM622/LVP-C composites with different loadings of LVP-C nanoparticles at 0.5 C was also compared (**Figure S5**). The NCM622/LVP-C (9:1) electrode displayed the best cycling performance in terms of stability and capacity among all electrodes due to the appropriate content of LVP-C. Meanwhile, the long-term cycling stability of two NCM622 and NCM622/LVP-C electrodes at a rate of 2 C was also compared (**Figure 3b**). The NCM622 electrode delivered a capacity of 103.9 mA h g⁻¹ after 200 cycles, retaining only 67.60% of its original value of 153.7 mA h g⁻¹. In contrast, the NCM622/LVP-C electrode presented a better cycle performance for which an initial discharge capacity of 149.6 mA h g⁻¹ was achieved, and 127.1 mA h g⁻¹ was maintained after 200 cycles, corresponding to a capacity retention of 85.0%, further suggesting the protective effect of the LVP-C layer. To confirm the positive role of LVP-C, the electrochemical performance of the LVP-C nanoparticles-based electrode also was tested and shown in **Figure S6**. The electrode showed stable cycling with negligible capacity decay for 100 and 200 cycles at 0.5 and 2 C, respectively, which suggests its superior cycling stability.

The morphologies of the NCM622 and NCM622/LVP-C electrodes after 50 cycles at 0.5 C were also characterized by SEM. Due to the formation of cathode electrolyte interphase (CEI), a common phenomenon on oxide cathodes, the intrinsic surface features of NCM622 and NCM622/LVP-C electrodes cannot be maintained. Nevertheless, different morphologies are still observed on the two samples. As shown in **Figure S7**, some microcracks and high surface roughness were observed in cycled NCM622 electrodes. In contrast, NCM622/LVP-C can maintain a relatively denser structure without some destructions, which can be attributed to the effective protection of LVP-C coating layer. This is likely due to the higher rate capability of LVP-C nanoparticles, which participate in lithiation and delithiation reaction earlier than NCM622 and serve as a buffer to release chemical and electrochemical stress built in the charge/discharge cycling.

Figure 3c and **3d** further compare the charge and discharge curves of the above two electrodes at 1, 10, 100, and 200 cycles. It can be observed that NCM622/LVP-C electrode shows similar curve shape to NCM622 electrode, which eliminates the multiple charge-discharge plateaus typically observed for LVP electrodes (**Figure S8**). This feature makes LVP-based electrodes more applicable for real applications due to easier monitoring of the state of charge. The average discharge voltage of NCM622 electrode declined faster than the NCM622/LVP-C electrode due to the stronger polarization

possibly originated from surface side reactions or microstructure changes during cycling. To investigate the electrode reaction process, CV profiles of two electrodes were compared at different cycles under 0.1 mV s^{-1} between 3.0-4.3 V. A pair of oxidation and reduction peaks at about 3.6-3.9 V can be found in all CV curves for NCM622 electrode, indicating the $\text{Ni}^{2+}/\text{Ni}^{4+}$ transformation of NCM622.³⁵ The current density became lower with the increase of cycle numbers due to the reduced electrochemical capacity (**Figure 3e**). For NCM622/LVP-C electrode, except the $\text{Ni}^{2+}/\text{Ni}^{4+}$ peaks, there are three couples of redox peaks in each CV profile, representing the extraction/insertion of two Li^+ in $\text{Li}_3\text{V}_2(\text{PO}_4)_3$ by three steps (Figure S5).³⁶ Furthermore, there is no obvious decrease of current density with increased cycle numbers, demonstrating better reversibility and higher cycling stability (**Figure 3f**). The NCM622/LVP-C electrode also displays the better rate capability than NCM622 electrodes, especially at high rates like 5C and 10C, suggesting that the composite electrodes are of great potential for fast charging batteries (**Figure S9**). EIS measurements were also performed for two electrodes after different cycles. As shown in **Figure S10** and **Table S1**, the NCM622/LVP-C electrode delivered a smaller ohmic resistance (R_s) and charge-transfer impedance (R_{ct}) than NCM622 electrode, leading to improved cycling stability due to the highly stable LVP-C coating.

To further confirm the improved rate performance by the composite electrode, Li^+ diffusion coefficient (D_{Li^+}) was calculated from the following equation (1)

$$D_{\text{Li}} = \frac{R^2 T^2}{2A^2 n^4 F^4 C^2 \sigma^2} \quad (1)$$

Where R is the gas constant ($8.314 \text{ J K}^{-1} \text{ mol}^{-1}$), T the absolute temperature (298 K), A the surface area of electrode, n the number of electrons transferred in the half-reaction for the redox reaction, F the Faraday constant (96500 C mol^{-1}), C the concentration of lithium ions and σ is the Warburg factor, which is based on Equation (2), and can be obtained from the slope of $Z' \sim \omega^{-1/2}$ plot as depicted in the **Figure S11**.

$$Z' = R_b + R_{sei} + R_{ct} + \sigma \omega^{-1/2} \quad (2)$$

The calculated D_{Li^+} values of the two electrodes are shown in **Table S2**. NCM622/LVP-C displays the higher D_{Li^+} (4.07×10^{-11}), which is about 3 times larger than that of NCM622 (1.23×10^{-11}). These results are consistent with its better rate performance of the NCM622/LVP-C electrode.

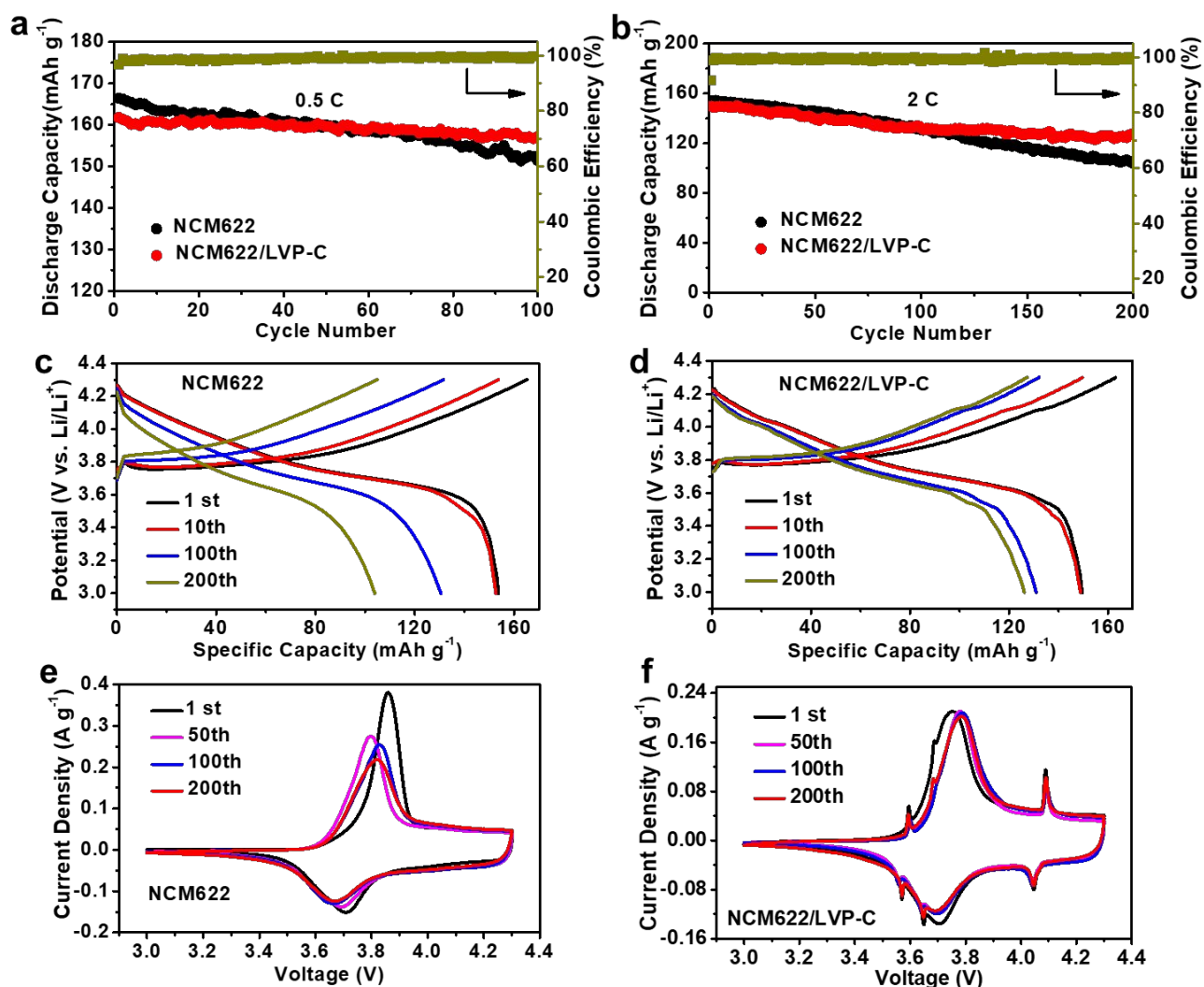


Figure 3 (a) Cycling performance of NCM622 electrode and NCM622/LVP-C electrode at current density of 0.5 C; (b) Cycling performance of NCM622 electrode and NCM622/LVP-C electrode at current density of 2.0 C; The charge and discharge curves of (c) NCM622 electrode and (d) NCM622/LVP-C electrode after different cycles; The CV curves of (e) NCM622 electrode and (f) NCM622/LVP-C electrode after different cycles at a scan rate of 0.1 mV s⁻¹ between 3.0-4.3V.

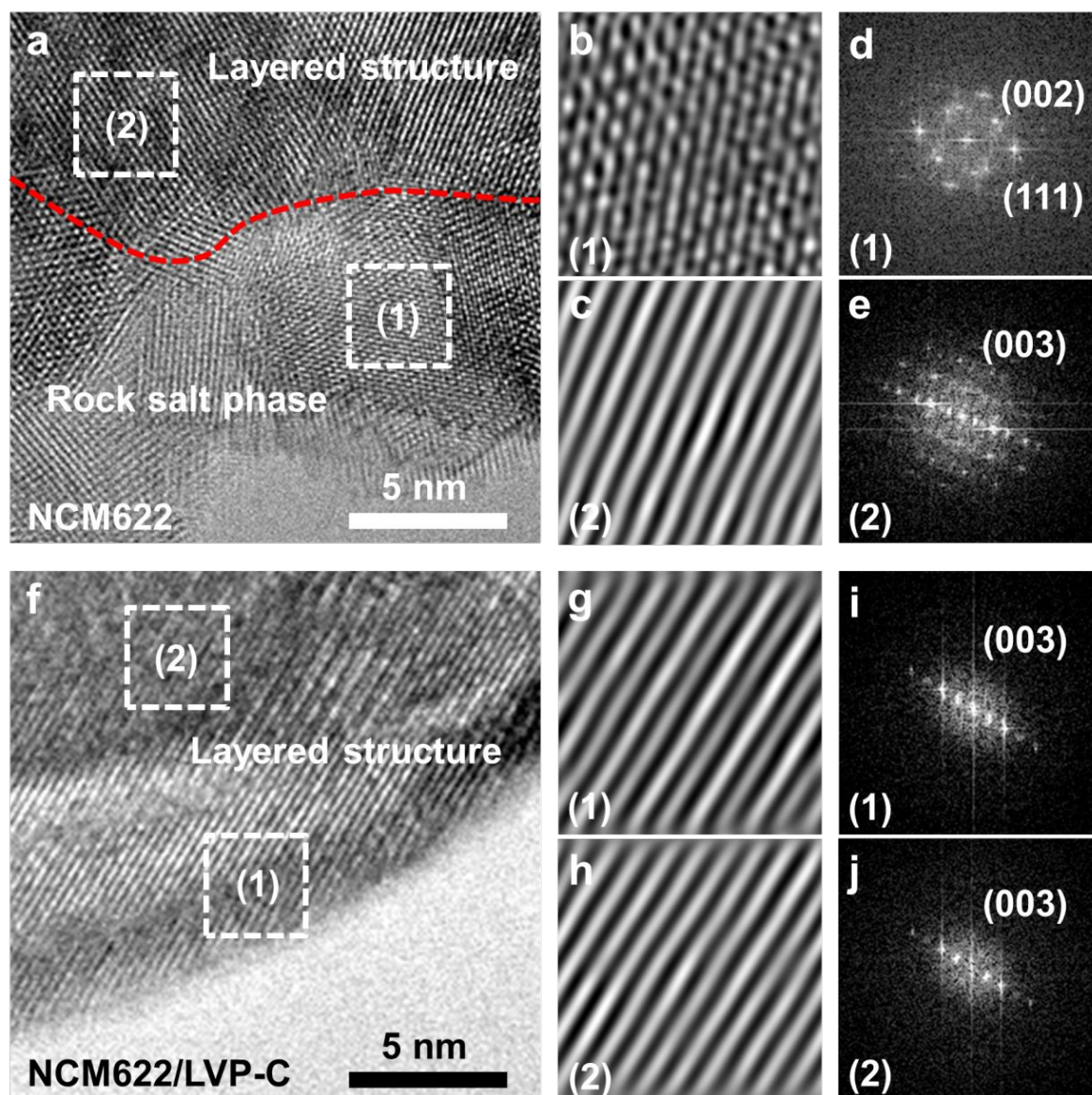


Figure 4 (a) HR-TEM image of the cycled NCM622 materials; FFT filtered TEM images recorded from (b) region 1 and (c) region 2 in (a); FFT results of (d) region 1 and (e) region 2 in (a); (f) HR-TEM image of the cycled NCM622/LVP-C composite; FFT filtered TEM images recorded from (g) region 1 and (h) region 2 in (f); FFT results of (i) region 1 and (j) region 2 in (f).

To investigate the structural changes of NCM622 and NCM622/LVP-C composite cathode after cycling, HR-TEM and Fast Fourier Transformation (FFT) were analyzed. **Figure 4a** presents the HR-TEM image of cycled NCM622 cathode particle, while **Figure 4b** and **c** show FFT filtered TEM images recorded from different selected areas in **Figure 4a**. FFT results from different regions indicate that the bulk of particles are layered phase (**Figure 4c**, region 2), while the surface of particles shows

some rock salt phase (**Figure 4b**, region 1). The characteristic spots in FFT pattern of rock salt phase can be indexed as (111) and (002) plane of NiO (**Figure 4d**), and layered phase refers to (003) plane (**Figure 4e**).³⁷ However, for NCM622/LVP-C composite, the structure of NCM622 remained to be its original layered structure in all regions (**Figure 4f-h**). Similarly, the FFT results also exhibit that NCM in the composite belongs to the (003) planes of α -NaFeO₂ layered structures (**Figure 4i and j**).³⁸ This microstructure analysis indicates that the LVP-C can effectively restrict undesired phase change of NCM622 during long cycling.

To further explore the microstructural evolutions after cycling, the XRD patterns of pristine NCM622, cycled NCM622 and cycled NCM622/LVP-C are compared in **Figure 5**. All the cycled cathodes displayed a typical pattern of the α -NaFeO₂ structure with $R\bar{3}m$ space group (**Figure 5a**). Due to the relatively small loading (10 wt.%), the LVP characteristic peaks were not observed in the composite cathode. It was also observed that compared to the pristine NCM622, the (003) peak of cycled NCM622 and NCM622/LVP-C shifts to the lower angles (**Figure 5b**) due to the loss of Li.³⁹ The cycled NCM622 cathode exhibited the lowest angles which corresponds to an increase in c lattice parameter because of the electrostatic repulsion between the oxygen layers along c directions in the Li-deficient state.⁴⁰ At the same time, the distance between the (108) peak and (110) peak increases after cycling, corresponding to the decrease in a lattice parameters due to the smaller effective ionic radii of Ni³⁺ than Ni²⁺ to compensate Li deficiency.⁴¹ The cycled NCM622 had a larger peak separation than cycled NCM622/LVP-C owing to the higher content of Ni²⁺. Rietveld refinement was carried out on all of the XRD patterns (**Figure S12**), and the lattice parameters were compared in **Table 2**. The refinement results further demonstrate that the cycled cathode particles have a smaller a lattice parameter and larger c lattice parameter than pristine NCM622. In addition, the cycled NCM622/LVP-C showed a lower Li/Ni mixing than cycled NCM622 (6.83% < 9.02%), which in agreement with HR-TEM results. Based on the analysis above, it is concluded that the LVP-C protective layer can effectively reduce the side reactions, inhibiting cation mixing of NCM622 and improving its structural stability, which leads to the improved cycling performance.

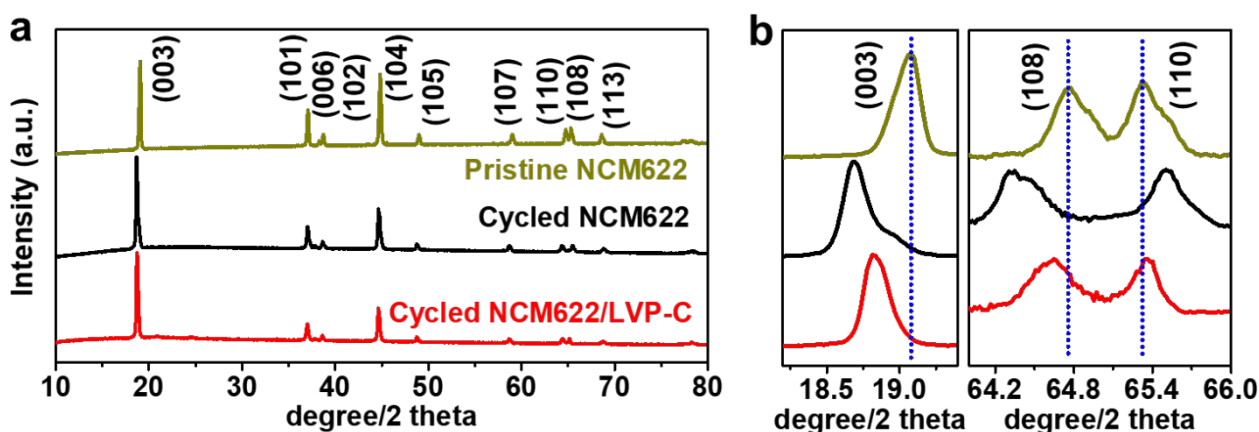


Figure 5 XRD patterns of pristine NCM622, cycled NCM622 and cycled NCM622/LVP-C in the ranges of (a) 10-80°; (b) 18.2-19.4 and 64-66°.

Table 2 The summary of fitting lattice parameters of pristine NCM622, cycled NCM622 and cycled NCM622/LVP-C.

Samples	$a / \text{Å}$	$c / \text{Å}$	Li/Ni mixing	R_{wp}	χ^2
Pristine NCM622	2.8627	14.1930	4.87%	1.42%	0.0086
Cycled NCM622	2.8578	14.3431	9.02%	3.61%	0.0496
Cycled NCM622/LVP-C	2.8601	14.2528	6.83%	3.43%	0.0256

To further demonstrate the potential application of the NCM622/LVP-C composites, full cells were assembled and tested with graphite as the anode. **Figure 6a** shows the cycling performance of different full cells at 0.5 C rate in the voltage range of 2.8-4.2 V. The full cell with NCM622/LVP-C cathode displayed an initial discharge capacity of 160.2 mA h g⁻¹ (based on the cathode mass) with a commercial-level areal capacity of 3.2 mA h cm⁻². The NCM622||graphite full cell delivered slightly higher initial capacity but with a more rapid capacity loss with a capacity retention of only 56.4% after 100 cycles. However, the NCM622/LVP-C||graphite full cell presented a significantly improved cycling stability with a capacity retention of 89.1% after 100 cycles. **Figure 6b and c** show the charge and discharge curves of full cells at different cycles. It can be clearly observed that the average voltage of NCM622 declines at a faster pace compared with NCM622/LVP-C due to the stronger polarization due to surface and/or structure instability induced during cycling. Without special electrolyte

formulation or cathode treatment, the drying coating of NCM622 by LVP-C nanoparticles helped to improve the cycling stability without sacrificing cell energy density, suggesting its potential as an effective, low-cost strategy to develop high-performance cathodes.

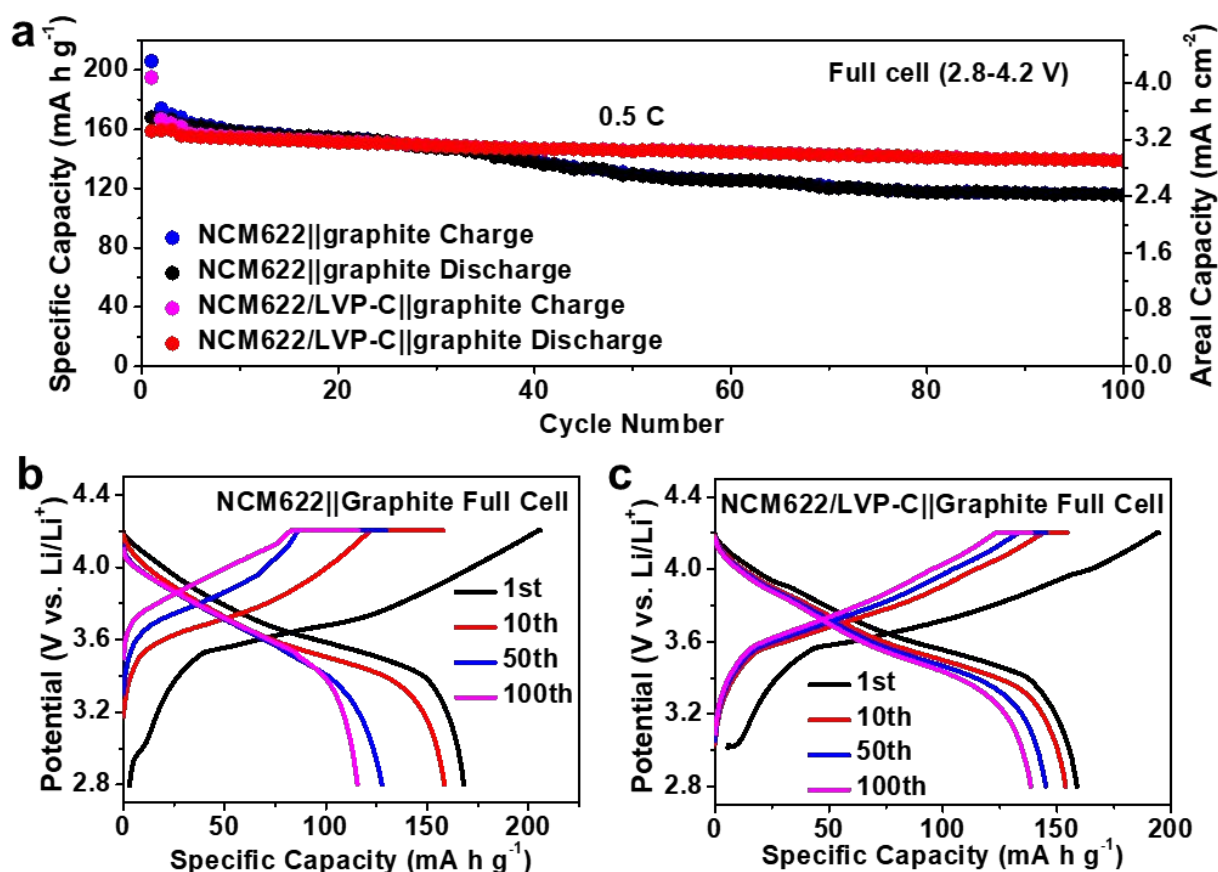


Figure 6 (a) The cycling performance of NCM622||graphite and NCM622/LVP-C||graphite full cells at 0.5 C between 2.8-4.2 V; The charge and discharge curves of (b) NCM622/LVP-C||graphite and (c) NCM622||graphite full cells at different cycles. Areal capacity as 3.2 mA h cm^{-2} for cathodes and the N/P ratio was controlled at 1.2.

4. Conclusions

In summary, we demonstrated a simple and effective drying coating method to synthesize NCM622/LVP-C composites, in which the micron-sized NCM622 secondary particles are uniformly protected by LVP-C nanoparticles. Due to the intrinsic structure stability of LVP and the uniform surface coating, such a composite cathode showed much better cycling stability than the pristine NCM622 cathode. Structure and morphology characterization showed that the LVP-C protective layer

can effectively reduce the side reactions, restrict the cation mixing of NCM622 cathode and improve its structural stability. With an optimal loading amount of the LVP-C nanoparticles, the NCM622/LVP-C composites can deliver a high specific capacity and excellent cycling performance, demonstrating its great promise for low-cost and high-performance cathodes. This method can be also extended to develop other composite cathode materials to further improve capacity and rate performance, making them more attractive for practical applications.

AUTHOR INFORMATION

Corresponding Author

*(Z.C.) E-mail: zhengchen@eng.ucsd.edu.

ORCID

Dongdong Wang: 0000-0002-0391-8242

Zhongqiang Shan: 0000-0001-5316-3186

Zheng Chen: 0000-0002-9186-4298

Notes

The authors declare no competing financial interest.

Acknowledgements

Z. Chen acknowledges the start-up fund support from UC San Diego. The support provided by China Scholarship Council during a visit of D. D. Wang to University of California San Diego is acknowledged (No. 201706250088) and China Postdoctoral Science Foundation (2020TQ0183). The transmission electron microscopy work by Q. Yan and J. Luo was supported as part of the Center for Synthetic Control Across Length-scales for Advancing Rechargeables (SCALAR), an Energy Frontier Research Center funded by the US DOE, Office of Science, BES under Award No. DESC0019381.

References

1. M. Armand and J.-M. Tarascon, *Nature*, 2008, **451**, 652-657.
2. J. B. Goodenough and K.-S. Park, *J. Am. Chem. Soc.*, 2013, **135**, 1167-1176.
3. D. Wang, H. Liu, M. Li, D. Xia and Z. Chen, *Nano Energy*, 2020, **75**, 104889.
4. D. Wang, G. Zhang, Z. Shan, T. Zhang and J. Tian, *ChemElectroChem*, 2018, **5**, 540-545.
5. D. Wang, Z. Shan, R. Na, W. Huang and J. Tian, *J. Power Sources*, 2016, **337**, 11-17.
6. Y. Shi, G. Chen, F. Liu, X. Yue and Z. Chen, *ACS Energy Letters*, 2018, **3**, 1683-1692.
7. W. Liu, P. Oh, X. Liu, M. J. Lee, W. Cho, S. Chae, Y. Kim and J. Cho, *Angew. Chem. Int. Ed.*, 2015, **54**, 4440-4457.
8. Y. Huang, X. Zhang and X. Wang, *ACS Appl. Mater. Interfaces*, 2019, **11**, 16556-16566.
9. Z. Chen, G.-T. Kim, Y. Guang, D. Bresser, T. Diemant, Y. Huang, M. Copley, R. J. Behm, S. Passerini and Z. Shen, *J. Power Sources*, 2018, **402**, 263-271.
10. F. Schipper, E. M. Erickson, C. Erk, J.-Y. Shin, F. F. Chesneau and D. Aurbach, *J. Electrochem. Soc.*, 2017, **164**, A6220-A6228.
11. P. Hou, J. Yin, M. Ding, J. Huang and X. Xu, *Small*, 2017, **13**, 1701802.
12. L. Cai, Z. Liu, K. An and C. Liang, *J. Electrochem. Soc.*, 2012, **159**, A924-A928.
13. L. Zhu, T.-F. Yan, D. Jia, Y. Wang, Q. Wu, H.-T. Gu, Y.-M. Wu and W.-P. Tang, *J. Electrochem. Soc.*, 2019, **166**, A5437-A5444.
14. H. Wang, W. Ge, W. Li, F. Wang, W. Liu, M.-Z. Qu and G. Peng, *ACS Appl. Mater. Interfaces*, 2016, **8**, 18439-18449.
15. Y. Chen, Y. Li, S. Tang, T. Lei, S. Deng, L. Xue, G. Cao and J. Zhu, *J. Power Sources*, 2018, **395**, 403-413.
16. Y. J. K. A, R. R. A, S. K. B and K. S. R. A, *Chem. Eng. J.*, 2020, **386**, 123975.
17. G. Song, H. Zhong, Z. Wang, Y. Dai and J. Yang, *ACS Applied Energy Materials*, 2019, **2**, 7923-7932.
18. X. Zhang, I. Belharouak, L. Li, Y. Lei, J. W. Elam, A. Nie, X. Chen, R. S. Yassar and R. L. Axelbaum, *Adv. Energy Mater.*, 2013, **3**, 1299-1307.
19. R. Wang, J. Wang, S. Chen, Q. Yuan and F. Wu, *Nano Energy*, 2020, **76**, 105065.
20. S. Jamil, G. Wang and X. Wang, *J Mater. Chem. A*, 2020, **8**, 21306-21316.
21. J. Duan, C. Wu, Y. Cao, K. Du, Z. Peng and G. Hu, *Electrochim. Acta*, 2016, **221**, 14-22.

22. Z. Wu, S. Ji, T. Liu, Y. Duan, S. Xiao, Y. Lin, K. Xu and F. Pan, *Nano Lett.*, 2016, **16**, 6357-6363.
23. X. Zhang, R.-S. Kühnel, H. Hu, D. Eder and A. Balducci, *Nano Energy*, 2015, **12**, 207-214.
24. C. Liu, R. Masse, X. Nan and G. Cao, *Energy Storage Mater.*, 2016, **4**, 15-58.
25. X.-K. Ding, L.-L. Zhang, X.-L. Yang, H. Fang, Y.-X. Zhou, J.-Q. Wang and D. Ma, *ACS Appl. Mater. Interfaces*, 2017, **9**, 42788-42796.
26. P. Sun, X. Zhao, R. Chen, T. Chen, L. Ma, Q. Fan, H. Lu, Y. Hu, Z. Tie and Z. Jin, *Nanoscale*, 2016, **8**, 7408-7415.
27. Q. Wei, Y. Xu, Q. Li, S. Tan, W. Ren, Q. An and L. Mai, *Chemical Communications*, 2016, **52**, 8730-8732.
28. R. Qin, Y. Wei, T. Zhai and H. Li, *J Mater. Chem. A*, 2018, **6**, 9737-9746.
29. T. Chen, J. Zhou, G. Fang, Y. Tang, X. Tan, A. Pan and S. Liang, *ACS Sustainable Chemistry & Engineering*, 2018, **6**, 7250-7256.
30. K. Naoi, K. Kisu, E. Iwama, Y. Sato, M. Shinoda, N. Okita and W. Naoi, *J. Electrochem. Soc.*, 2015, **162**, A827-A833.
31. D. Wang, Z. Shan and J. Tian, *ChemNanoMat*, 2020, **6**, 1-7.
32. H. Wang, Y. Li, C. H. Huang, Y. Zhong and S. Liu, *J. Power Sources*, 2012, **208**, 282-287.
33. L.-L. Zhang, Z. Li, X.-L. Yang, X.-K. Ding, Y.-X. Zhou, H.-B. Sun, H.-C. Tao, L.-Y. Xiong and Y.-H. Huang, *Nano Energy*, 2017, **34**, 111-119.
34. C. Liu, S. Wang, C. Zhang, H. Fu, X. Nan, Y. Yang and G. Cao, *Energy Storage Mater.*, 2016, **5**, 93-102.
35. J. Fu, D. Mu, B. Wu, J. Bi, H. Cui, H. Yang, H. Wu and F. Wu, *ACS Appl. Mater. Interfaces*, 2018, **10**, 19704-19711.
36. Y. Liao, C. Li, X. Lou, X. Hu, Y. Ning, F. Yuan, B. Chen, M. Shen and B. Hu, *Electrochim. Acta*, 2018, **271**, 608-616.
37. Y. Shi, M. Zhang, Y. S. Meng and Z. Chen, *Adv. Energy Mater.*, 2019, **9**, 1900454.
38. F. Wu, Q. Li, L. Chen, Y. Lu, Y. Su, L. Bao, R. Chen and S. Chen, *ChemSusChem*, 2019, **12**, 935-943.
39. Y. Shi, M. Zhang, Y. S. Meng and Z. Chen, *Adv. Energy Mater.*, 2019, **9**.
40. D. Mohanty, S. Kalnaus, R. A. Meisner, K. J. Rhodes, J. Li, E. A. Payzant, D. L. Wood III

and C. Daniel, *J. Power Sources*, 2013, **229**, 239-248.

41. D. Mohanty and H. Gabrisch, *J. Power Sources*, 2012, **220**, 405-412.